The geometry of the hot corona in MCG-05-23-16 constrained by X-ray polarimetry

D. Tagliacozzo, A. Marinucci, F. Ursini, G. Matt, S. Bianchi, L. Baldini, T. Barnouin, N. Cavero Rodriguez, A. De Rosa, L. Di Gesu, et al.

▶ To cite this version:

D. Tagliacozzo, A. Marinucci, F. Ursini, G. Matt, S. Bianchi, et al.. The geometry of the hot corona in MCG-05-23-16 constrained by X-ray polarimetry. Monthly Notices of the Royal Astronomical Society, 2023, 10.1093/mnras/stad2627 . insu-04202386

HAL Id: insu-04202386
https://insu.hal.science/insu-04202386v1

Monthly Notices
of the
ROYAL ASTRONOMICAL SOCIETY

MNRAS **525,** 4735–4743 (2023)
Advance Access publication 2023 September 1

https://doi.org/10.1093/mnras/stad2627

The geometry of the hot corona in MCG-05-23-16 constrained by X-ray polarimetry

D. Tagliacozzo,[1★] A. Marinucci,[2] F. Ursini,[1] G. Matt,[1] S. Bianchi,[1] L. Baldini,[3,4] T. Barnouin,[5] N. Cavero Rodriguez,[6] A. De Rosa,[7] L. Di Gesu,[2] M. Dovčiak,[8] D. Harper,[6] A. Ingram,[9] V. Karas,[8] D. E. Kim,[7,10,11] H. Krawczynski,[6] G. Madejski,[12] F. Marin,[5] R. Middei,[13,14] H. L. Marshall,[15] F. Muleri,[7] C. Panagiotou,[15] P.-O. Petrucci,[16] J. Podgorny,[5,8,17] J. Poutanen,[18] S. Puccetti,[14] P. Soffitta,[7] F. Tombesi,[11,19,20] A. Veledina,[18,21] W. Zhang,[22] I. Agudo,[23] L. A. Antonelli,[13,14] M. Bachetti,[24] W. H. Baumgartner,[25] R. Bellazzini,[3] S. D. Bongiorno,[25] R. Bonino,[26,27] A. Brez,[3] N. Bucciantini,[28,29,30] F. Capitanio,[7] S. Castellano,[3] E. Cavazzuti,[2] C.-T. Chen,[31] S. Ciprini,[14,19] E. Costa,[7] E. Del Monte,[7] N. Di Lalla,[12] A. Di Marco,[7] I. Donnarumma,[2] V. Doroshenko,[32] S. R. Ehlert,[25] T. Enoto,[33] Y. Evangelista,[7] S. Fabiani,[7] R. Ferrazzoli,[7] J. A. Garcia,[34] S. Gunji,[35] J. Heyl,[36] W. Iwakiri,[37] S. G. Jorstad,[38,39] P. Kaaret,[25] F. Kislat,[40] T. Kitaguchi,[33] J. J. Kolodziejczak,[25] F. La Monaca,[7] L. Latronico,[26] I. Liodakis,[41] S. Maldera,[26] A. Manfreda,[42] A. P. Marscher,[38] F. Massaro,[26,27] I. Mitsuishi,[43] T. Mizuno,[44] M. Negro,[45,46,47] C.-Y. Ng,[48] S. L. O'Dell,[25] N. Omodei,[12] C. Oppedisano,[26] A. Papitto,[13] G. G. Pavlov,[49] A. L. Peirson,[12] M. Perri,[13,14] M. Pesce-Rollins,[3] M. Pilia,[24] A. Possenti,[24] B. D. Ramsey,[25] J. Rankin,[7] A. Ratheesh,[7] O. J. Roberts,[31] R. W. Romani,[12] C. Sgrò,[3] P. Slane,[50] G. Spandre,[3] D. A. Swartz,[31] T. Tamagawa,[33] F. Tavecchio,[51] R. Taverna,[52] Y. Tawara,[43] A. F. Tennant,[25] N. E. Thomas,[25] A. Trois,[24] S. S. Tsygankov,[18] R. Turolla,[52,53] J. Vink,[54] M. C. Weisskopf,[25] K. Wu,[53] F. Xie[7,55] and S. Zane[53]

Affiliations are listed at the end of the paper

Accepted 2023 July 28. Received 2023 July 19; in original form 2023 May 17

ABSTRACT

We report on the second observation of the radio-quiet active galactic nucleus MCG-05-23-16 performed with the *Imaging X-ray Polarimetry Explorer* (*IXPE*). The observation started on 2022 November 6 for a net observing time of 640 ks, and was partly simultaneous with *NuSTAR* (86 ks). After combining these data with those obtained in the first *IXPE* pointing on 2022 May (simultaneous with *XMM–Newton* and *NuSTAR*) we find a 2–8 keV polarization degree $\Pi = 1.6 \pm 0.7$ (at 68 per cent confidence level), which corresponds to an upper limit $\Pi = 3.2$ per cent (at 99 per cent confidence level). We then compare the polarization results with Monte Carlo simulations obtained with the MONK code, with which different coronal geometries have been explored (spherical lamppost, conical, slab, and wedge). Furthermore, the allowed range of inclination angles is found for each geometry. If the best-fitting inclination value from a spectroscopic analysis is considered, a cone-shaped corona along the disc axis is disfavoured.

Key words: polarization – galaxies: active – galaxies: Seyfert – X-rays: galaxies – X-rays: individual: MCG-05-23-16.

1 INTRODUCTION

The large amount of energy released by active galactic nuclei (AGNs) is widely thought to be generated in a very compact and central region via accretion on to a supermassive black hole (SMBH, Rees 1984; Antonucci 1993). The optical/UV radiation emitted by the accretion disc is partly redirected towards the X-ray band (primary emission) through a process known as Comptonization, which involves multiple scatterings in a cloud of hot electrons, generally called the corona (Sunyaev & Titarchuk 1980; Haardt & Maraschi 1991; Zdziarski, Poutanen & Johnson 2000; Zdziarski & Gierlinski 2004; Done, Gierliński & Kubota 2007). These structures are characterized by high electron temperatures (kT_e usually ranging from tens to hundreds keV) and moderate Thomson optical depths (τ, Petrucci et al. 2001; Perola et al. 2002; Dadina 2007; Panessa et al. 2011; De Rosa et al. 2012; Ricci et al. 2017; Marinucci et al. 2018; Tortosa et al. 2018; Middei et al. 2019). Despite being a key element in understanding the energy generation mechanism of AGNs, the morphology of the corona, which may hold clues to its physical

---

★ E-mail: daniele.tagliacozzo@uniroma3.it

Published by Oxford University Press on behalf of Royal Astronomical Society

origins, remains a matter of debate. While in principle spectroscopic techniques can provide information on the coronal geometry, even the best observations, while providing valuable information on its physical parameters such as temperature and optical depth, fall short of distinguishing between different geometrical configurations (Tortosa et al. 2018; Zhang, Dovčiak & Bursa 2019). Currently, some constraints on the coronal morphology have been derived using time lags techniques (such as reverberation mapping, Uttley et al. 2014; Fabian et al. 2017; Caballero-García et al. 2020), but many aspects remain to be determined. In this context, X-ray polarimetry represents a fundamental tool in order to investigate the coronal properties and constrain its geometry, because different morphologies of the emitting region produce different polarization signatures.

Several geometrical models have been proposed for the corona. In this work we consider the following: spherical lamppost, conical outflow, slab corona, and wedge-shaped hot accretion flow. The spherical lamppost consists of an isotropic spherical source located on the spin axis of the SMBH (Matt, Perola & Piro 1991; Wilkins & Fabian 2012; Ursini et al. 2022) and it is defined by its radius and its height above the SMBH. This configuration is expected to produce a low polarization degree (PD = 0–2 per cent) with the polarization angle (PA) perpendicular to the accretion disc axis (Ursini et al. 2022). The conical outflow is commonly associated with an aborted jet (Henri & Petrucci 1997; Ghisellini, Haardt & Matt 2004; Ursini et al. 2022). According to this model, radio-quiet AGNs have central SMBHs powering outflows and jets which may propagate only for a short distance, if the velocity of the ejected material is sub-relativistic and smaller than the escape velocity. This configuration is expected to produce somewhat larger (up to 6 per cent) polarization degree, also in this case perpendicular to the accretion disc axis (Ursini et al. 2022). In the slab corona scenario the hot medium is assumed to be uniformly distributed above the cold accretion disc. This geometry can be realized in the scenario where magnetic loops rise high above the disc plane and dissipate energy via reconnection (Liang 1979; Haardt & Maraschi 1991; Beloborodov 2017). This configuration can produce polarization degree up to 14 per cent (Poutanen & Svensson 1996; Ursini et al. 2022; Gianolli et al. 2023). In this case the polarization angle is parallel to the accretion disc axis. The wedge is, finally, similar to the slab but with the height increasing with the radius. In this scenario the 'standard' accretion disc is thought to be truncated at a certain radius, while the corona represents some type of a 'hot accretion flow', possibly extending to the innermost stable circular orbit (ISCO, Esin, McClintock & Narayan 1997; Poutanen, Krolik & Ryde 1997; Schnittman & Krolik 2010; Yuan & Narayan 2014; Poutanen, Veledina & Zdziarski 2018; Ursini et al. 2020). It is expected to produce intermediate (up to 5 per cent, depending on the specific assumed configuration) polarization degree, parallel to the accretion disc axis. This configuration is considered in detail in Section 4.

MCG-05-23-16 is a nearby ($z = 0.0085$, Wegner et al. 2003) Seyfert 1.9 galaxy (Veron et al. 1980) with broad emission lines in the infrared (Goodrich, Veilleux & Hill 1994). It is a relatively bright X-ray source ($F_{2\text{–}10} = 7\text{–}10 \times 10^{-11}\,\mathrm{erg\,cm^{-2}\,s^{-1}}$, Mattson & Weaver 2004) showing moderate cold absorption ($N_{\rm H} \sim 10^{22}\,\mathrm{cm^{-2}}$). It has been widely studied in the X-ray band (Beckmann et al. 2008; Molina et al. 2013), and its high-energy cut-off ($E_{\rm C}$) and coronal physical parameters, i.e. temperature and Thomson optical depth, are quite well estimated (Baloković et al. 2015). The SMBH mass ($M_{\rm BH} = 2 \times 10^7\,\mathrm{M_\odot}$) has been estimated via X-ray variability (Ponti et al. 2012), and it is consistent with the virial mass derived from the infrared lines (Onori et al. 2017). From the observations of MCG-05-23-16 performed with *XMM–Newton*, *NuSTAR*, and *IXPE* in 2022 May, Marinucci et al. (2022) found, assuming a simple cut-off power law for the primary continuum, a spectral index $\Gamma = 1.85 \pm 0.01$ and a high-energy cut-off $E_{\rm C} = 120 \pm 15$ keV, leading to an electron temperature $kT_{\rm e} = 25 \pm 2$ keV and $\tau = 1.27 \pm 0.08$ if the cut-off power law is replaced by the comptonization model COMPPS (Poutanen & Svensson 1996) and a uniform slab geometry for the corona is assumed. Moreover, a 4.7 per cent upper limit (99 per cent c.l. for one parameter of interest) for the polarization degree was obtained.

In this paper we present and discuss the second *IXPE* observation of MCG-5-23-16, performed in 2022 November in coordination with *NuSTAR*. The combined analysis of the data collected in the 2022 May and November observations is also discussed. The results are then compared with Monte Carlo simulations of the expected polarization properties for different geometries of the corona.

The paper is organized as follows: in Section 2 we discuss the data reduction procedure, in Section 3 we present the spectropolarimetric data analysis, in Section 4 we present Monte Carlo simulations designed to calculate the expected polarization for different geometries and, finally, the results are summarized in Section 5.

2 OBSERVATIONS AND DATA REDUCTION

IXPE (Weisskopf et al. 2022) observed MCG-05-23-16 twice, in 2022 May and November. The first *IXPE* observation and the simultaneous *XMM–Newton* and *NusTAR* data are presented in Marinucci et al. (2022). These spectra, with updated response matrices, are also used in this work. The second pointing started on November 6, and had a net exposure time of 642 ks. Cleaned level 2 event files were produced and calibrated using standard filtering criteria with the dedicated FTOOLS tasks and the latest calibration files available in the *IXPE* calibration data base (CALDB 20220303). I, Q, and U Stokes background spectra were extracted from source-free circular regions with a radius of 100 arcsec. Extraction radii for the I Stokes spectra of the source were computed via an iterative process which leads to the maximization of the signal-to-noise ratio (SNR) in the 2–8 keV energy band, similar to the approach described in Piconcelli et al. (2004). We therefore adopted circular regions centred on the source with radii of 62 arcsec for the three Detector Units (DUs). The net exposure times are 641.7 ks and the same extraction radii were then applied to the Q and U Stokes spectra. We used a constant energy binning of 0.2 keV for Q and U Stokes spectra and required an SNR higher than 5 in each spectral channel, in the intensity spectra. I, Q, and U Stokes spectra from the three DUs are always fitted independently in the following, but we will plot them together using the SETP GROUP command in XSPEC, for the sake of visual clarity. Background represents 2.0, 1.8, and 2.1 per cent of the total DU1, DU2, and DU3 I spectra, respectively. We followed the formalism discussed in Strohmayer (2017) and used the weighted analysis method presented in Di Marco et al. (2022) (parameter STOKES = NEFF in XSELECT). The summed background-subtracted light curves for the two *IXPE* pointings are shown in Fig. 1.

NuSTAR (Harrison et al. 2013) observed MCG-05-23-16, with its two coaligned X-ray telescopes with corresponding Focal Plane Module A (FPMA) and B (FPMB), on 2022 November 11. The total elapsed time is 164.6 ks. The Level 1 data products were processed with the *NuSTAR* Data Analysis Software (NuSTARDAS) package (v. 2.1.2). Cleaned event files (level 2 data products) were produced and calibrated using standard filtering criteria with the NUPIPELINE task and the latest calibration files available in the *NuSTAR* calibration data base (CALDB 20221020). Extraction radii for the source and background spectra were 40 and 60 arcsec, FPMA spectra were

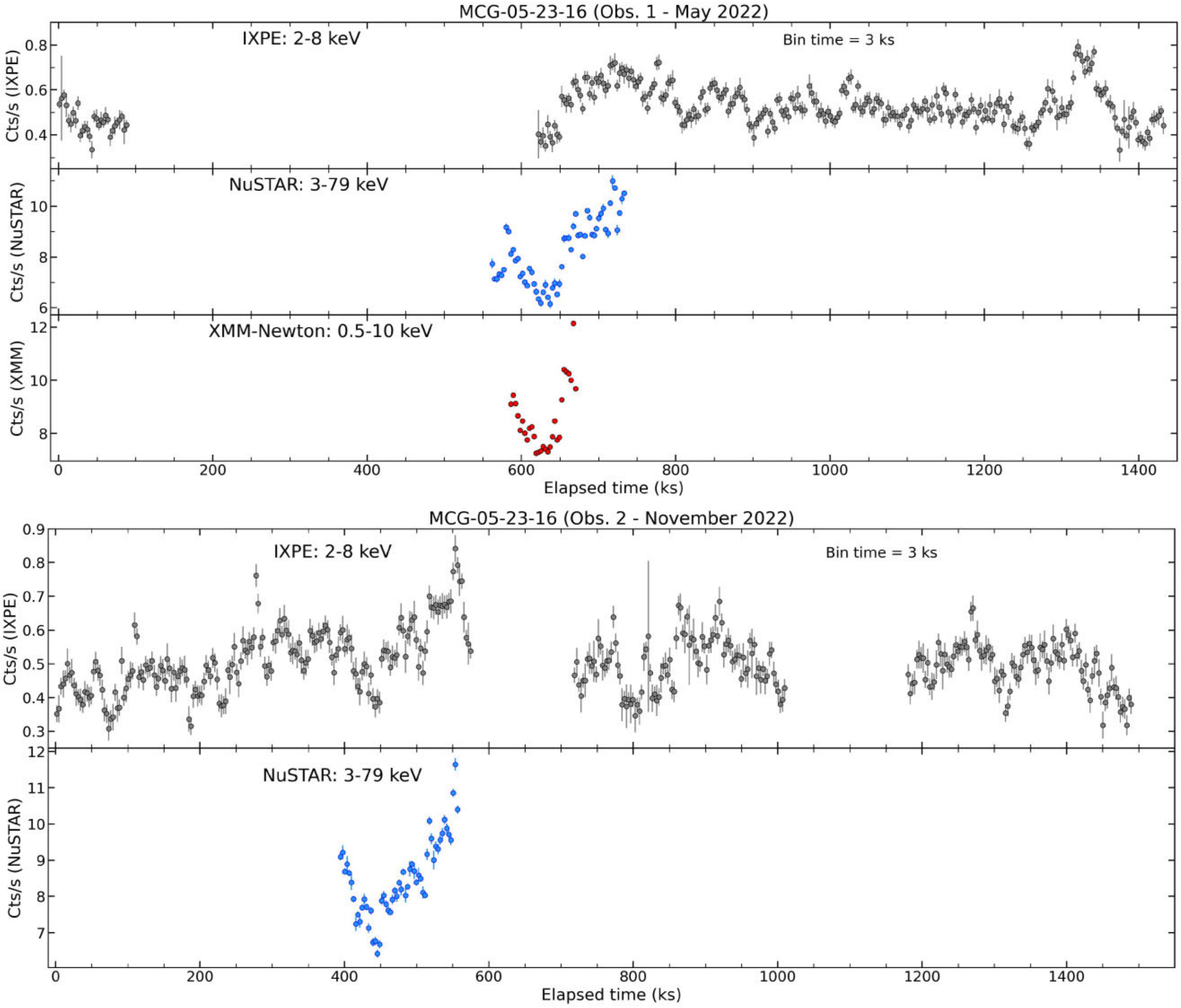

Figure 1. *IXPE*, *NuSTAR*, and *XMM–Newton* light curves of the two observing campaign of MCG-05-23-16 are shown. Data counts from DU1, DU2, and DU3 onboard the *IXPE* and from FPMA/B onboard the *NuSTAR* have been summed. The full energy bands of the three satellites have been used and we adopted a 3 ks time binning.

binned in order not to oversample the instrumental resolution more than a factor of 2.5 and to have an SNR greater than 5 in each spectral channel; the same energy binning was then applied to the FPMB spectra. The net observing times for the FPMA and the FPMB data sets are 85.7 and 84.9 ks, respectively. The summed background-subtracted FPMA and FPMB light curves are shown in Fig. 1. We adopt the cosmological parameters $H_0 = 70$ km s^{-1} Mpc^{-1}, $\Omega_\Lambda = 0.73$, and $\Omega_\mathrm{m} = 0.27$, i.e. the default ones in XSPEC 12.12.1 (Arnaud 1996). Errors correspond to the 90 per cent confidence level for one interesting parameter ($\Delta\chi^2 = 2.7$), if not stated otherwise.

3 DATA ANALYSIS

3.1 *IXPE* analysis

Initially, we conducted a preliminary examination of the *IXPE* data through the utilization of a baseline model, consisting of an absorbed power law convolved with a constant polarization kernel: CONST × POLCONST × TBABS × POWERLAW. We fit this model in the 2–8 keV energy range simultaneously to the I, Q, and U spectra collected by the three *IXPE* DUs during the second observation of MCG-05-23-16 (2022 November 6; 640 ks). In all cases where we only use *IXPE* data the adoption of a more complex model is unnecessary. In fact, the reduced chi-square is always close to unity. At the 68 per cent c.l. for one parameter of interest, we obtained a polarization degree $\Pi = 1.1 \pm 0.9$ per cent and a polarization angle $\Psi = 57^\circ \pm 27^\circ$. This translates into a 99 per cent c.l. upper limit to the polarization degree of $\Pi = 3.3$ per cent. In Fig. 2 we show the Q and U spectra used to perform this first analysis (along with the model and the residuals), while in Fig. 3 the contour plot between Π and Ψ is shown. An alternative model-independent analysis of the polarization cubes with the software IXPEOBSSIM (Baldini et al. 2022) gives consistent results.

We then performed a combined analysis of the *IXPE* I, Q, and U spectra collected on 2022 May and November, using the same model. We notice a significant variation of the primary continuum spectral index between the two pointings. This variation is only found in the *IXPE* data. For this reason, we consider it as a calibration issue concerning the first pointing of MCG-05-23-16 by this instrument. For this reason, it is not possible to sum the two observations together.

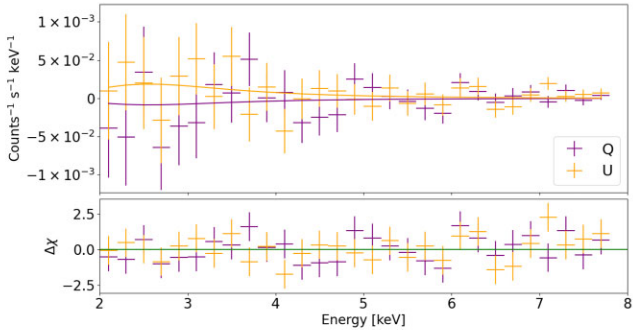

Figure 2. *IXPE Q* (purple crosses) and *U* (orange crosses) grouped Stokes spectra of the second *IXPE* pointing (2022 November) of MCG-05-23-16 are shown with residuals, along with the corresponding best-fitting model.

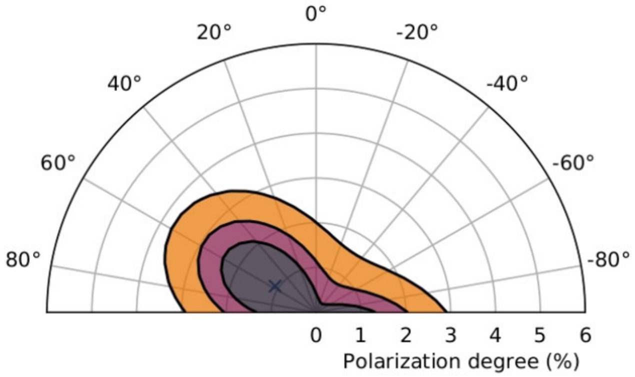

Figure 3. Contour plot between the polarization degree Π and angle Ψ for the 2022 November data. The purple, pink, and orange regions correspond, respectively, to 68, 90, and 99 per cent confidence levels for two parameters of interest.

Table 1. Polarimetric properties of MCG-05-23-16 obtained with *IXPE*.

Parameter	2022 May	2022 Nov	2022 May + Nov
Π (per cent)	2.2 ± 1.7	1.1 ± 0.9	1.6 ± 0.7
Ψ (deg)	50 ± 24	57 ± 27	53 ± 13
Π upper limit (per cent)	≤ 4.7	≤ 3.3	≤ 3.2

Note. The errors are shown at 68 per cent and the upper limits at 99 per cent confidence level for one parameter of interest.

We therefore proceeded to conduct a combined analysis leaving untied the spectral indexes of the two pointings. We obtained (at 68 per cent c.l. for one interesting parameter) a polarization degree $\Pi = 1.6 \pm 0.7$ per cent and a polarization angle $\Psi = 53^\circ \pm 13^\circ$. This translates into a polarization degree upper limit (at 99 per cent c.l.) $\Pi = 3.2$ per cent. This represents a significant improvement with respect to the results obtained for the 2022 May observation alone. In Table 1 the best-fitting values of the polarization degree and angle obtained using only *IXPE* data set are shown.

3.2 *XMM–Newton*, *NuSTAR*, and *IXPE* combined analysis

As a next step we performed a spectropolarimetric analysis combining the 2–8 keV *IXPE* spectra (May + November), the 2–10 keV *XMM–Newton* spectrum (May), and the 3–79 keV *NuSTAR* spectra (May + November). Taking advantage of the previous analysis of the May observations (Marinucci et al. 2022), we used the following model:

CONST × TBABS[POLCONST × ZTBABS × CUTOFFPL+
VASHIFT(POLCONST × KERRDISK + POLCONST × XILLVER)],

where the constant component is needed to cross-calibrate the data set collected by the different detectors (DU1, DU2, DU3, FPMA, FPMB, and EPIC pn). The primary continuum is modelled using a simple power law with a high-energy exponential cut-off (CUTOFFPL), while TBABS is used to model the Galactic absorption, using a column density $N_{\rm H} = 7.8 \times 10^{20}$ cm^{-2} (HI4PI Collaboration 2016). The reflection from distant (and neutral) material (such as the external regions of the accretion disc and the torus) is modelled using XILLVER (García et al. 2013). The spectral index and high-energy cut-off in the reflection model are linked to those of the primary emission. The Fe abundance is set equal to the solar value and the inclination angle to $\theta = 30^\circ$. The KERRDISK component (Brenneman & Reynolds 2006) is used to deal with some residuals close to 6.4 keV, which may be interpreted as a Fe Kα line from the inner part of the accretion disc, broadened by relativistic effects. For the *XMM–Newton* spectrum we added a VASHIFT component (which simply provides a shift in energy) in order to deal with the energy of the narrow Fe Kα line, which is inconsistent with being 6.4 keV in the host galaxy rest frame. This effect is only found in the pn (and not in the MOS), so we conclude that it is likely due to calibration issues. We noticed a similar effect also in *NuSTAR*, with an increasing deviation between the first and the second pointing. For this reason, we added a VASHIFT component here too, attributing the effect to instrument degradation in time. In KERRDISK, the black hole spin is fixed to $a = 0.998$, since the fit is largely insensitive to this parameter. Moreover, we fixed the disc emissivity profile to $\epsilon(r) \propto r^{-3}$. The rest-frame energy of the line was fixed to 6.4 keV and the inner radius of the disc to its previously found best-fitting value ($37R_{\rm G}$, as found by Reeves et al. 2007).[1] In order to deal with calibration issues that affect the spectral index of May *IXPE* observation, we modified, as in Marinucci et al. (2022), the response files gain in the *I* spectra (using the GAIN FIT command). Finally, as done for the *IXPE* analysis, we untied the primary continuum spectral indices between the two observations.

Each main spectral component (i.e. primary continuum and reflection) is associated with a different polarization. The Fe Kα line is expected to be unpolarized (Goosmann & Matt 2011; Marin 2018), while the Compton reflection continuum contributes little in the *IXPE* band pass (Marin, Dovčiak & Kammoun 2018). For these reasons, after checking the insensitivity of the fit to variations of these parameters, we fix the polarization of KERRDISK and XILLVER to zero for simplicity (see also Marinucci et al. 2022). We get only an upper limit (at 99 per cent c.l. for one interesting parameter) for the polarization degree of the primary continuum of $\Pi = 3.3$ per cent. At 68 per cent of c.l., we retrieve a polarization degree and angle of $\Pi = 1.6 \pm 0.7$ per cent and $\Psi = 53^\circ \pm 12^\circ$, respectively. The fit is not ideal (χ^2/dof=2381/2259, see Fig. 4) but, since there is no evidence from the residuals of missing or wrong components in the model, we attribute it to an imperfect cross calibration between the three instruments.

In Table 2 we summarize the best-fitting values for all the free parameters of this last and complete analysis (with errors at 68 per cent

---

[1] A complete and detailed spectroscopic analysis of these data sets, including the relativistic effects, will be presented in a forthcoming paper (Serafinelli et al, in preparation).

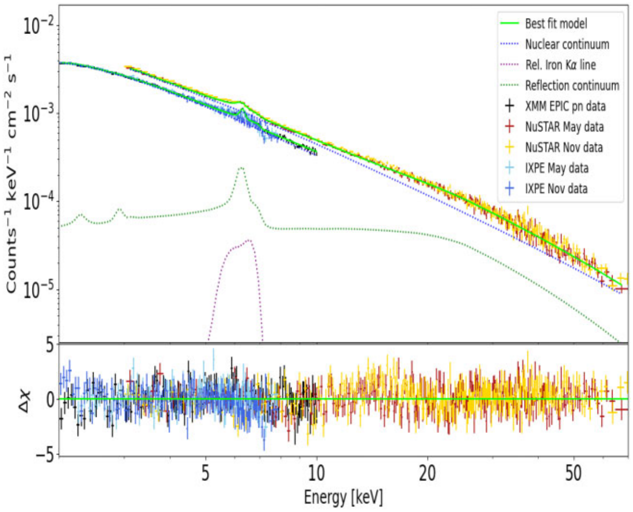

Figure 4. The EPIC pn (2022 May), *NuSTAR* (2022 May + November), and *IXPE I* (2022 May + November) spectra together with the best-fitting model (*upper panel*), and the residuals (*lower panel*).

Table 2. Best-fitting parameters for the *XMM–Newton*, *NuSTAR*, and *IXPE* 2022 May + November combined data set.

Parameter	Best-fitting value
$N_{\rm H}$ (cm^{-2})	$(1.30 \pm 0.02) \times 10^{22}$
$\Gamma_{\rm CUTOFFPL}$ (May)	1.84 ± 0.01
$\Gamma_{\rm CUTOFFPL}$ (Nov)	1.85 ± 0.01
$E_{\rm C}$ (keV)	120^{+9}_{-5}
$\Pi_{\rm CUTOFFPL}$ (per cent)	1.6 ± 0.7
$\Psi_{\rm CUTOFFPL}$ (deg)	53 ± 12
$\Pi_{\rm XILL} = \Pi_{\rm KERR}$ (per cent)	0
$\Psi_{\rm XILL} = \Psi_{\rm KERR}$ (deg)	0
$v_{\rm shift}$ (km s^{-1})	
XMM–Newton	$2.2^{+0.3}_{-0.4} \times 10^{3}$
NuSTAR (May)	$3.4^{+0.9}_{-0.4} \times 10^{3}$
NuSTAR (Nov)	$5.5^{+1.0}_{-0.8} \times 10^{3}$
$\theta_{\rm KERR}$ (deg)	61^{+4}_{-13}
a	0.998
$R_{\rm in}$ ($R_{\rm G}$)	37
$\theta_{\rm incl}$ (deg)	30
Normalization constants	
$N_{\rm CUTOFFPL}$	$(2.52 \pm 0.02) \times 10^{-2}$
$N_{\rm XILL}$	$(2.0 \pm 0.1) \times 10^{-4}$
$N_{\rm KERR}$	$(3.6 \pm 0.3) \times 10^{-5}$
F_{2-10} (erg cm^{-2}s^{-1})	
XMM–Newton	$(7.48 \pm 0.01) \times 10^{-11}$
NuSTAR (Nov)	$(1.12 \pm 0.02) \times 10^{-10}$
L_{2-10} (erg s^{-1})	$(1.70 \pm 0.01) \times 10^{43}$
R	0.42 ± 0.03
χ^2/dof	2381/2259

Note. The errors at 68 per cent c.l. for one parameter of interest. Π and Ψ of XILLVER and KERRDISK are set equal to 0. Parameters without error have been frozen in the fit. The spectral index for the first observation is obtained applying the GAIN FIT command. R is the reflection fraction defined as the ratio between the 20–40 keV fluxes of the Compton reflection and the primary component.

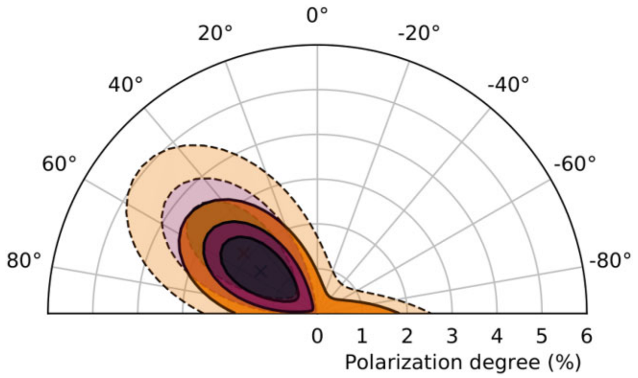

Figure 5. Comparison between the polarization degree Π and angle Ψ contour plots from the combined (2022 May + November) observations *XMM–Newton*, *NuSTAR*, and *IXPE* (*continuous line-saturated plot*) and the first (2022 May) observation only (*dashed line-pale plot*). The purple, pink, and orange regions represent, respectively, the 68, 90, and 99 per cent confidence levels for two parameters of interest.

c.l.). In Fig. 5 we show the contour plot of the polarization degree and angle of the continuum component, as well as a comparison with the contour plot from the May observation alone (Marinucci et al. 2022).

4 MONTE CARLO SIMULATIONS

To interpret the polarization results, we perform detailed numerical simulations with the Monte Carlo code MONK (Zhang et al. 2019), following the approach of Ursini et al. (2022) (where spherical lamppost, conical outflow, and slab have been already explored). We focus here on the so-called concave wedge geometry which, similarly to the slab, gives rise to polarization angles parallel to the accretion disc axis. A wedge configuration could potentially solve some of the theoretical issues that arise when using geometries such as the slab or the sphere (Stern et al. 1995; Done et al. 2007; Poutanen et al. 2018). The wedge geometry is defined by three parameters: an inner radius ($R_{\rm in}$), an outer radius ($R_{\rm out}$), and an opening angle (α) (see Fig. 6). We assume the inner radius to coincide with the ISCO, which depends on the SMBH spin value (6 $R_{\rm G}$ for $a = 0$ and 1.24 $R_{\rm G}$ for $a = 0.998$). Unlike the slab configuration, the height of the wedge increases with radius. In this configuration the accretion disc is assumed to be truncated at a certain radius, while the corona represents a ‘hot accretion flow’, extending to the ISCO. The density profile of the wedge corona is uniform and the Thomson optical depth is computed radially. Finally, the accretion disc truncation radius can either coincide with the external edge of the corona or reach lower values, down to the ISCO. In Fig. 6 a sketch of the wedge corona is shown.

We perform Monte Carlo simulations for a total of eight parameter combinations, considering only the external disc scenario with uniform coronal density (a detailed analysis of the various wedge configurations is beyond the scope of this paper and will be presented in a following paper). The simulations are run for two values of the SMBH spin ($a = 0$ and $a = 0.998$). In both cases, we set the inner radius to the ISCO, i.e. 6 $R_{\rm G}$ for the static black hole and 1.24 $R_{\rm G}$ for the maximally rotating black hole. We test four different opening angles (15°, 30°, 45°, and 60°). We set the coronal electron temperature to 25 keV, as measured by Baloković et al. (2015) and Marinucci et al. (2022). After setting the electron temperature, for each geometrical configuration we find the optical depth that fits

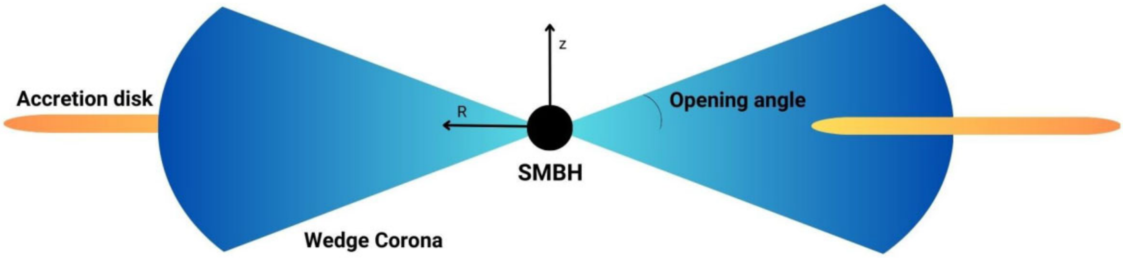

Figure 6. The wedge corona. This geometry is characterized by an inner and an outer radius and an opening angle (measured from the accretion disc plane). In the left configuration, the inner radius of the accretion disc coincides with the outer radius of the corona, while in the right configuration it extends into the corona itself. The *R* and *z* axes represent the radial and the vertical coordinates.

Table 3. Coronal input parameters for the MONK simulations.

kT_e (keV)	SMBH spin	R_{in} (R_G)	α (deg)	τ	PD$_{max}$ (per cent)
25	0	6	15	6.8	5
			30	4.2	4
			45	3.3	3
			60	2.8	2.3
	0.998	1.24	15	8.3	5.8
			30	5.1	4.3
			45	3.8	3.2
			60	3.2	3.2

Note. In the last column the maximum polarization degree (PD$_{max}$) resulting from the simulations is reported.

the spectrum best in the *IXPE* band pass (i.e. 2–8 keV) when we replace the cut-off power law with the spectra obtained with MONK in the best-fitting model retrieved in Section 3.2. In Table 3 we summarize the physical and geometrical parameters we assume in the simulations. For all the simulations we perform, we assume a mass of the SMBH of $M_{\rm BH} = 2 \times 10^7 M_\odot$ and an Eddington ratio of 0.1 (Ponti et al. 2012). Finally, we set the initial polarization (i.e. the polarization of the optical/UV radiation emitted by the accretion disc) as appropriate for a pure scattering, plane-parallel, semi-infinite atmosphere (Chandrasekhar 1960).

The polarization angle is found to be always parallel to the accretion disc axis. The degree of polarization is up to 5–6 per cent for the smaller opening angles, showing no significant variations with energy in the 2–8 keV energy range. In all tested cases, we notice a decrease in the degree of polarization for larger opening angles, as the geometry becomes closer to a sphere, for which zero polarization is expected. Finally, we notice a slight increase in PD between the static and the maximum spinning black hole cases. In Fig. 7 we show the polarization degree as a function of the cosine of the inclination angle ($\mu = \cos\theta_{\rm disc}$).

5 CONCLUSIONS

Constraining the geometry of the comptonizing corona in AGNs is one of the main goals of *IXPE*. So far, three radio-quiet, unobscured AGNs have been observed: MCG-05-23-16 (Marinucci et al. 2022), NGC 4151 (Gianolli et al. 2023), and IC 4329A (Ingram et al. in preparation). The first observation of MCG-05-23-16 put constraints on the polarization degree of the primary continuum ($\Pi \le 4.7$ per cent) and found a hint of alignment between the polarization angle and the accretion disc spin axis. In NGC 4151 a clear detection has been obtained, with a polarization degree of $\Pi = 4.9 \pm 1.1$ per cent and a polarization angle parallel to the disc axis (as probed by the radio jet). These results disfavour a lamppost geometry (Gianolli et al. 2023)

In this paper we have analysed the second pointing of MCG-05-23-16 performed by *IXPE* on 2022 November, also combining this observation with the first one (2022 May), and using *XMM–Newton* and *NuSTAR* data taken contemporaneously. The results were then compared with theoretical simulations performed with the Comptonization Monte Carlo code MONK. The combined analysis led to a significant decrease of the upper limit to the polarization degree of the primary continuum, which is now $\Pi \le 3.2$ per cent (to be compared with $\Pi \le 4.7$ per cent from the first observation only, Marinucci et al. 2022).

Hubble Space Telescope's WFPC2 images showed that the ionization cone of MCG-05-23-16 has a roughly 40° position angle, as probed by [O III] emission (Ferruit, Wilson & Mulchaey 2000). Let us assume it as a marker for the narrow-line region (NLR), and that the NLR elongation axis is perpendicular to the accretion disc. Even if the polarization angle is formally unconstrained, given that we do not have a firm polarization detection, our analysis nevertheless suggests a statistical preference for a polarization angle in the ∼50° direction (see Fig. 5). This is a hint that the polarization of the primary emission is aligned with the NLR and so parallel to the accretion disc axis, similar to what was found in NGC 4151 (Gianolli et al. 2023).

Let us now use the PD–PA contour plots to put constraints on the geometrical parameters of the corona. In Fig. 8 we plot, superimposed to the contour plots, the polarization degree and angle from MONK simulations for four different geometries. The results for the lamppost, cone, and slab are taken from Ursini et al. (2022) and all assume a static black hole, a coronal temperature of 25 keV, and the optical depth which best reproduces the observed MCG-05-23-16 spectrum analysed by Marinucci et al. (2022). In the absence of any independent constraint on the source inclination, we cannot formally exclude any geometry, as, for low enough angles, any of them can reproduce a polarization degree close to zero. For the slab and the wedge cases (which have polarization angles parallel to the disc axis), the effective upper limit is 3.2 per cent, and we can constrain the source inclination to be lower than 40° assuming the slab geometry. If we instead assume the wedge geometry, the allowed range of source inclinations depends also on opening angle α. We see from Fig. 7 that for $\alpha \gtrsim 45°$, the predicted polarization degree is always below our observational upper limit, thus leaving the source inclination unconstrained. On the other hand, assuming a static SMBH constrains the inclination to be either below 50° or above 80° for $\alpha = 30°$ and to be lower than 50° for $\alpha = 15°$. Assuming instead a maximally spinning SMBH constrains the inclination to be lower than about 40° for both $\alpha = 30°$ and $\alpha = 15°$.

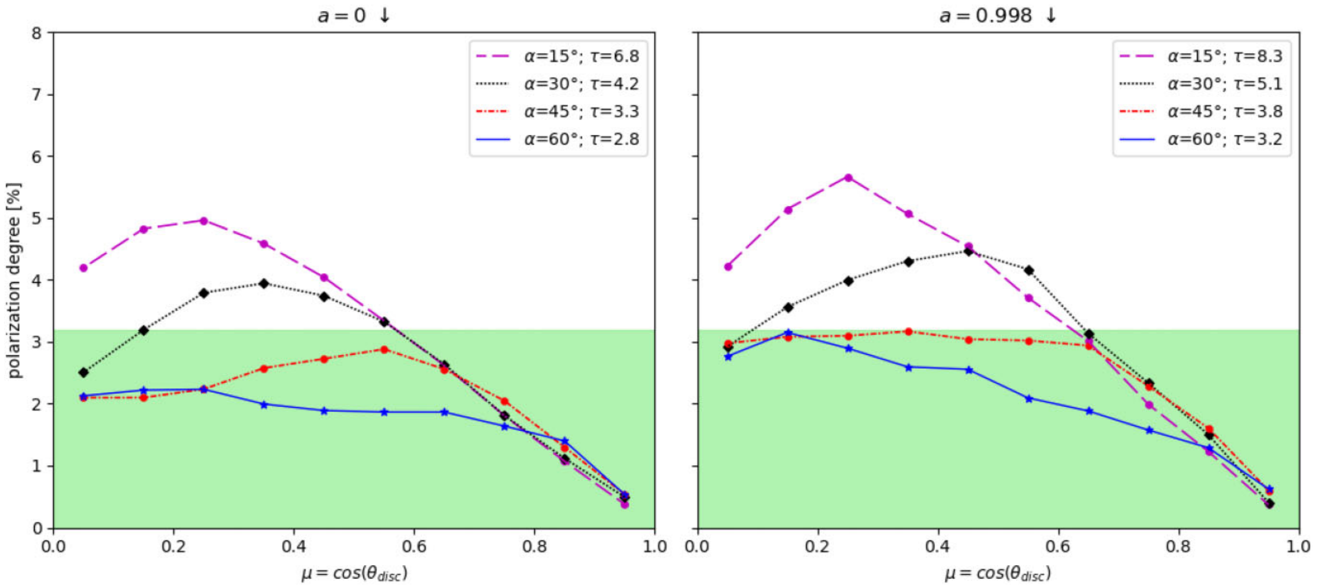

Figure 7. Polarization degree from the MONK simulations in the case of a wedge-shaped corona as a function of the cosine of the inclination angle ($\mu = \cos\theta_{\rm disc}$, where $\mu = 0$ and $\mu = 1$ represent the edge-on and face-on views of the source, respectively. *Left panel*: static SMBH ($a = 0$) cases. *Right panel*: maximally spinning SMBH ($a = 0.998$). The purple, black, red, and blue lines correspond to the 15°, 30°, 45°, and 60° opening angles cases, respectively). The green regions represent the allowed values of the polarization degree (see Section 3.2).

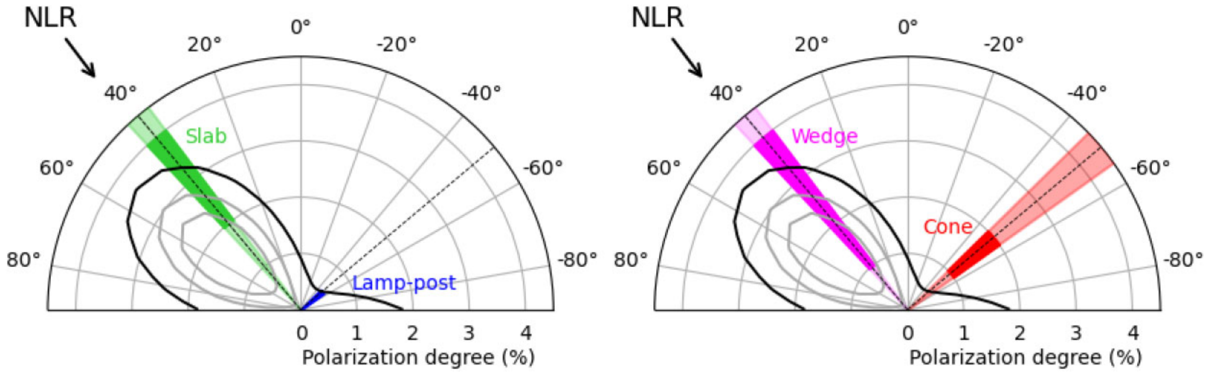

Figure 8. Comparison between MONK simulations and the contour plot of the combined analysis presented in Section 3.2. Different coronal geometries are shown: slab (in light green) and spherical lamppost (in blue) in the *left panel*, wedge (in magenta) and cone (in red) in the *right panel*. Regions of the plot filled with pale colours represent the expected Π for all the possible inclinations of the source, while the saturated ones represent the expected degree for inclinations in the range 30°–50°, as found in Serafinelli et al. (in preparation). The black-dotted line at 40° represents the supposed elongation of the NLR (which is the expected polarization angle in the slab and wedge geometries), while the black-dotted line at −50° represents the direction orthogonal to the NLR, (the expected polarization angle for the lamppost and the cone).

For coronal geometries that predict polarization angles perpendicular to the disc axis, the upper limit on polarization degree is much more stringent ($\Pi \leq 0.5$ per cent). In this scenario, if we consider the cone-shaped corona, we can constrain the source inclination to be lower than 20°. Finally, considering the lamppost geometry, since it predicts a very low PD for all inclinations, no constraints could be obtained. Information on the inclination angle, however, can in principle be obtained by modelling the reflection component. Serafinelli at al. (in preparation) found the inclination of MCG-05-23-16 to be constrained in the 30°–50° range. If we assume these values, Fig. 8 shows that the cone-shaped corona is disfavoured.

ACKNOWLEDGEMENTS

The *Imaging X ray Polarimetry Explorer* (*IXPE*) is a joint US and Italian mission. The US contribution is supported by the National Aeronautics and Space Administration (NASA) and led and managed by its Marshall Space Flight Center (MSFC), with industry partner Ball Aerospace (contract NNM15AA18C). The Italian contribution is supported by the Italian Space Agency (ASI) through contract ASI-OHBI-2017-12-I.0, agreements ASI-INAF-2017-12-H0 and ASI-INFN-2017.13-H0, and its Space Science Data Center (SSDC), and by the Istituto Nazionale di Astrofisica (INAF) and the Istituto Nazionale di Fisica Nucleare (INFN) in Italy. This research used data products provided by the *IXPE* Team (MSFC, SSDC, INAF, and INFN) and distributed with additional software tools by the High-Energy Astrophysics Science Archive Research Center (HEASARC), at NASA Goddard Space Flight Center (GSFC). Part of the French contribution is supported by the Scientific Research National Center (CNRS) and the French Space Agency (CNES). MD, VK, and JPod thank for the support from the GACR project 21-06825X and the institutional support from RVO:67985815. IA acknowledges financial support from the Spanish ‘Ministerio de Ciencia e Innovación’ (MCINN) through the ‘Center of Excellence Severo Ochoa’ award for the Instituto de Astrofísica de Andalucía-CSIC (SEV-2017-0709) and through grants AYA2016-80889-P and PID2019-107847RB-C44. We thank the referee, A. Zoghbi, for constructive comments that improved the paper.

DATA AVAILABILITY

The data analysed in this work are either publicly available at the HEASARC data base or available from the corresponding author upon request.

REFERENCES

Antonucci R., 1993, ARA&A, 31, 473

Arnaud K. A., 1996, in Jacoby G. H., Barnes J., eds, ASP Conf. Ser. Vol. 101, Astronomical Data Analysis Software and Systems V. Astron. Soc. Pac., San Francisco, p. 17

Baldini L. et al., 2022, SoftwareX, 19, 101194

Baloković M. et al., 2015, ApJ, 800, 62

Beckmann V., Courvoisier T. J. L., Gehrels N., Lubiński P., Malzac J., Petrucci P. O., Shrader C. R., Soldi S., 2008, A&A, 492, 93

Beloborodov A. M., 2017, ApJ, 850, 141

Brenneman L. W., Reynolds C. S., 2006, ApJ, 652, 1028

Caballero-García M. D., Papadakis I. E., Dovčiak M., Bursa M., Svoboda J., Karas V., 2020, MNRAS, 498, 3184

Chandrasekhar S., 1960, Radiative Transfer. Dover, New York

Dadina M., 2007, A&A, 461, 1209

De Rosa A. et al., 2012, MNRAS, 420, 2087

Di Marco A. et al., 2022, AJ, 163, 170

Done C., Gierliński M., Kubota A., 2007, A&AR, 15, 1

Esin A. A., McClintock J. E., Narayan R., 1997, ApJ, 489, 865

Fabian A. C., Alston W. N., Cackett E. M., Kara E., Uttley P., Wilkins D. R., 2017, Astron. Nachr., 338, 269

Ferruit P., Wilson A. S., Mulchaey J., 2000, ApJS, 128, 139

García J., Dauser T., Reynolds C. S., Kallman T. R., McClintock J. E., Wilms J., Eikmann W., 2013, ApJ, 768, 146

Ghisellini G., Haardt F., Matt G., 2004, A&A, 413, 535

Gianolli V. E. et al., 2023, MNRAS, 523, 4468

Goodrich R. W., Veilleux S., Hill G. J., 1994, ApJ, 422, 521

Goosmann R. W., Matt G., 2011, MNRAS, 415, 3119

Haardt F., Maraschi L., 1991, ApJ, 380, L51

Harrison F. A. et al., 2013, ApJ, 770, 103

Henri G., Petrucci P. O., 1997, A&A, 326, 87

HI4PI Collaboration, 2016, A&A, 594, A116

Liang E. P. T., 1979, ApJ, 231, L111

Marin F., 2018, A&A, 615, A171

Marin F., Dovčiak M., Kammoun E. S., 2018, MNRAS, 478, 950

Marinucci A. et al., 2022, MNRAS, 516, 5907

Marinucci A., Tamborra F., Bianchi S., Dovčiak M., Matt G., Middei R., Tortosa A., 2018, Galaxies, 6, 44

Matt G., Perola G. C., Piro L., 1991, A&A, 247, 25

Mattson B. J., Weaver K. A., 2004, ApJ, 601, 771

Middei R., Bianchi S., Marinucci A., Matt G., Petrucci P. O., Tamborra F., Tortosa A., 2019, A&A, 630, A131

Molina M., Bassani L., Malizia A., Stephen J. B., Bird A. J., Bazzano A., Ubertini P., 2013, MNRAS, 433, 1687

Onori F. et al., 2017, MNRAS, 468, L97

Panessa F. et al., 2011, MNRAS, 417, 2426

Perola G. C., Matt G., Cappi M., Fiore F., Guainazzi M., Maraschi L., Petrucci P. O., Piro L., 2002, A&A, 389, 802

Petrucci P. O. et al., 2001, ApJ, 556, 716

Piconcelli E., Jimenez-Bailón E., Guainazzi M., Schartel N., Rodríguez-Pascual P. M., Santos-Lleó M., 2004, MNRAS, 351, 161

Ponti G., Papadakis I., Bianchi S., Guainazzi M., Matt G., Uttley P., Bonilla N. F., 2012, A&A, 542, A83

Poutanen J., Svensson R., 1996, ApJ, 470, 249

Poutanen J., Krolik J. H., Ryde F., 1997, MNRAS, 292, L21

Poutanen J., Veledina A., Zdziarski A. A., 2018, A&A, 614, A79

Rees M. J., 1984, ARA&A, 22, 471

Reeves J. N. et al., 2007, PASJ, 59, 301

Ricci C. et al., 2017, ApJS, 233, 17

Schnittman J. D., Krolik J. H., 2010, ApJ, 712, 908

Stern B. E., Poutanen J., Svensson R., Sikora M., Begelman M. C., 1995, ApJ, 449, L13

Strohmayer T. E., 2017, ApJ, 838, 72

Sunyaev R. A., Titarchuk L. G., 1980, A&A, 86, 121

Tortosa B. S., Marinucci A., Matt G., Petrucci P. O., 2018, A&A, 614, A37

Ursini F. et al., 2020, A&A, 634, A92

Ursini F., Matt G., Bianchi S., Marinucci A., Dovčiak M., Zhang W., 2022, MNRAS, 510, 3674

Uttley P., Cackett E. M., Fabian A. C., Kara E., Wilkins D. R., 2014, A&AR, 22, 72

Veron P., Lindblad P. O., Zuiderwijk E. J., Veron M. P., Adam G., 1980, A&A, 87, 245

Wegner G. et al., 2003, AJ, 126, 2268

Weisskopf M. C. et al., 2022, J. Astron. Telesc. Instrum. Syst., 8, 026002

Wilkins D. R., Fabian A. C., 2012, MNRAS, 424, 1284

Yuan F., Narayan R., 2014, ARA&A, 52, 529

Zdziarski A. A., Gierlinski M., 2004, Prog. Theor. Phys. Suppl., 155, 99

Zdziarski A. A., Poutanen J., Johnson W. N., 2000, ApJ, 542, 703

Zhang W., Dovčiak M., Bursa M., 2019, ApJ, 875, 148

[1] *Dipartimento di Matematica e Fisica, Università degli Studi Roma Tre, via della Vasca Navale 84, I-00146 Roma, Italy*

[2] *Agenzia Spaziale Italiana, Via del Politecnico snc, I-00133 Roma, Italy*

[3] *Istituto Nazionale di Fisica Nucleare, Sezione di Pisa, Largo B. Pontecorvo 3, I-56127 Pisa, Italy*

[4] *Dipartimento di Fisica, Università di Pisa, Largo B. Pontecorvo 3, I-56127 Pisa, Italy*

[5] *CNRS, Observatoire Astronomique de Strasbourg, Université de Strasbourg, UMR 7550, F-67000 Strasbourg, France*

[6] *Physics Department and McDonnell Center for the Space Sciences, Washington University in St Louis, St Louis, MO 63130, USA*

[7] *INAF Istituto di Astrofisica e Planetologia Spaziali, Via del Fosso del Cavaliere 100, I-00133 Roma, Italy*

[8] *Astronomical Institute of the Czech Academy of Sciences, Boční II 1401/1, CZ-14100 Praha 4, Czech Republic*

[9] *School of Mathematics, Statistics, and Physics, Newcastle University, Newcastle upon Tyne NE1 7RU, UK*

[10] *Dipartimento di Fisica, Università degli Studi di Roma ‘La Sapienza,’ Piazzale Aldo Moro 5, I-00185 Roma, Italy*

[11] *Dipartimento di Fisica, Università degli Studi di Roma ‘Tor Vergata’, Via della Ricerca Scientifica 1, I-00133 Roma, Italy*

[12] *Department of Physics and Kavli Institute for Particle Astrophysics and Cosmology, Stanford University, Stanford, CA 94305, USA*

[13] *INAF Osservatorio Astronomico di Roma, Via Frascati 33, I-00040 Monte Porzio Catone (RM), Italy*

[14] *Space Science Data Center, Agenzia Spaziale Italiana, Via del Politecnico snc, I-00133 Roma, Italy*

[15] *MIT Kavli Institute for Astrophysics and Space Research, Massachusetts Institute of Technology, 77 Massachusetts Avenue, Cambridge, MA 02139, USA*

[16] *IPAG, CNRS, Université Grenoble Alpes, F-38000 Grenoble, France*

[17] *Astronomical Institute, Charles University, V Holešovickách 2, CZ-18000 Prague, Czech Republic*

[18] *Department of Physics and Astronomy, University of Turku, FI-20014 Turku, Finland*

[19] *Istituto Nazionale di Fisica Nucleare, Sezione di Roma ‘Tor Vergata’, Via della Ricerca Scientifica 1, I-00133 Roma, Italy*

[20]*Department of Astronomy, University of Maryland, College Park, MD 20742, USA*
[21]*Nordita, KTH Royal Institute of Technology and Stockholm University, Hannes Alfvéns väg 12, SE-10691 Stockholm, Sweden*
[22]*National Astronomical Observatories, Chinese Academy of Sciences, 20A Datun Road, Beijing 100101, China*
[23]*Instituto de Astrofísicade Andalucía – CSIC, Glorieta de la Astronomía s/n, E-18008 Granada, Spain*
[24]*INAF Osservatorio Astronomico di Cagliari, Via della Scienza 5, I-09047 Selargius (CA), Italy*
[25]*NASA Marshall Space Flight Center, Huntsville, AL 35812, USA*
[26]*Istituto Nazionale di Fisica Nucleare, Sezione di Torino, Via Pietro Giuria 1, I-10125 Torino, Italy*
[27]*Dipartimento di Fisica, Università degli Studi di Torino, Via Pietro Giuria 1, I-10125 Torino, Italy*
[28]*INAF Osservatorio Astrofisico di Arcetri, Largo Enrico Fermi 5, I-50125 Firenze, Italy*
[29]*Dipartimento di Fisica e Astronomia, Università degli Studi di Firenze, Via Sansone 1, I-50019 Sesto Fiorentino (FI), Italy*
[30]*Istituto Nazionale di Fisica Nucleare, Sezione di Firenze, Via Sansone 1, I-50019 Sesto Fiorentino (FI), Italy*
[31]*Science and Technology Institute, Universities Space Research Association, Huntsville, AL 35805, USA*
[32]*Institut für Astronomie und Astrophysik, Universität Tübingen, Sand 1, D-72076 Tübingen, Germany*
[33]*RIKEN Cluster for Pioneering Research, 2-1 Hirosawa, Wako, Saitama 351-0198, Japan*
[34]*California Institute of Technology, Pasadena, CA 91125, USA*
[35]*Yamagata University,1-4-12 Kojirakawa-machi, Yamagata-shi 990-8560, Japan*
[36]*University of British Columbia, Vancouver, BC V6T 1Z4, Canada*
[37]*International Center for Hadron Astrophysics, Chiba University, Chiba 263-8522, Japan*
[38]*Institute for Astrophysical Research, Boston University, 725 Commonwealth Avenue, Boston, MA 02215, USA*
[39]*Department of Astrophysics, St Petersburg State University, Universitetsky pr. 28, Petrodvoretz, St Petersburg 198504, Russia*
[40]*Department of Physics and Astronomy and Space Science Center, University of New Hampshire, Durham, NH 03824, USA*
[41]*Finnish Centre for Astronomy with ESO, 20014 University of Turku, FI-20014 Turku, Finland*
[42]*Istituto Nazionale di Fisica Nucleare, Sezione di Napoli, Strada Comunale Cinthia, I-80126 Napoli, Italy*
[43]*Graduate School of Science, Division of Particle and Astrophysical Science, Nagoya University, Furo-cho, Chikusa-ku, Nagoya, Aichi 464-8602, Japan*
[44]*Hiroshima Astrophysical Science Center, Hiroshima University, 1-3-1 Kagamiyama, Higashi-Hiroshima, Hiroshima 739-8526, Japan*
[45]*University of Maryland, Baltimore County, Baltimore, MD 21250, USA*
[46]*NASA Goddard Space Flight Center, Greenbelt, MD 20771, USA*
[47]*Center for Research and Exploration in Space Science and Technology, NASA/GSFC, Greenbelt, MD 20771, USA*
[48]*Department of Physics, University of Hong Kong, Pokfulam, Hong Kong*
[49]*Department of Astronomy and Astrophysics, Pennsylvania State University, University Park, PA 16801, USA*
[50]*Center for Astrophysics, Harvard & Smithsonian, 60 Garden St, Cambridge, MA 02138, USA*
[51]*INAF Osservatorio Astronomico di Brera, via E. Bianchi 46, I-23807 Merate (LC), Italy*
[52]*Dipartimento di Fisica e Astronomia, Università degli Studi di Padova, Via Marzolo 8, I-35131 Padova, Italy*
[53]*Mullard Space Science Laboratory, University College London, Holmbury St Mary, Dorking, Surrey RH5 6NT, UK*
[54]*Anton Pannekoek Institute for Astronomy & GRAPPA, University of Amsterdam, Science Park 904, NL-1098 XH Amsterdam, the Netherlands*
[55]*Guangxi Key Laboratory for Relativistic Astrophysics, School of Physical Science and Technology, Guangxi University, Nanning 530004, China*

This paper has been typeset from a TEX/LATEX file prepared by the author.

Published by Oxford University Press on behalf of Royal Astronomical Society